

## XMM-NEWTON REVEALS THE QUASAR OUTFLOW IN PG 1115+080

G. CHARTAS,<sup>1</sup> W. N. BRANDT,<sup>1</sup> AND S. C. GALLAGHER<sup>1,2</sup>  
*Received 2003 March 3; accepted 2003 June 3*

### ABSTRACT

We report on an observation of the Broad Absorption Line (BAL) quasar PG 1115+080 performed with the *XMM-Newton* observatory. Spectral analysis reveals the second case of a relativistic X-ray absorbing outflow in a BAL quasar. The first case was revealed in a recent observation of APM 08279+5255 with the *Chandra* X-ray Observatory. As in the case of APM 08279+5255, the observed flux of PG 1115+080 is greatly magnified by gravitational lensing. The relatively high redshift ( $z = 1.72$ ) of the quasar places the redshifted energies of resonant absorption features in a sensitive portion of the *XMM-Newton* spectral response. The spectrum indicates the presence of complex low-energy absorption in the 0.2–0.6 keV observed energy band and high-energy absorption in the 2–5 keV observed energy band. The high-energy absorption is best modeled by two Gaussian absorption lines with rest-frame energies of 7.4 keV and 9.5 keV. Assuming that these two lines are produced by resonant absorption due to Fe xxv  $K\alpha$ , we infer that the X-ray absorbers are outflowing with velocities of  $\sim 0.10c$  and  $\sim 0.34c$ , respectively. We have detected significant variability of the energies and widths of the X-ray BALs in PG 1115+080 and APM 08279+5255 over timescales of 19 and 1.8 weeks (proper-time), respectively. The BAL variability observed from APM 08279+5255 supports our earlier conclusion that these absorbers are most likely launched at relatively small radii of  $\lesssim 10^{16}(M_{BH}/M_{\odot})^{1/2}$  cm. A comparison of the ionization properties and column densities of the low-energy and high-energy absorbers indicates that these absorbers are likely distinct; however, higher spectral resolution is needed to confirm this result. Finally, we comment on prospects for constraining the kinematic and ionization properties of these X-ray BALs with the next generation of X-ray observatories.

*Subject headings:* galaxies: active — quasars: absorption lines — quasars: individual (PG 1115+080)  
— quasars: individual (APM 08279+5255) — X-rays: galaxies — gravitational lensing

### 1. INTRODUCTION

Most of our current understanding of the kinematic structure in Broad Absorption Line quasar (BALQSO) outflows stems from numerous studies of the velocity structures of BAL features that appear blueward of resonant UV emission lines. The similarities between the emission-line properties of quasars with and without BAL features led Weymann et al. (1991) to conclude that BALQSOs are “normal” quasars with a BAL global covering factor of  $\sim 10\%$ , viewed along lines of sight that traverse the outflowing UV absorbers. In this model, quasar winds exist in most quasars; however, because of the relatively small opening angles of these outflows only a small fraction of radio-quiet quasars have detectable BAL features in their UV and/or optical spectra. Spectropolarimetric observations, the statistics of gravitationally lensed BALQSOs, improved assessments of incompleteness, and theoretical arguments suggest that present optical surveys may be biased against the detection of BALQSOs (e.g., Goodrich 1997; Chartas 2000; Krolik & Voit 1998; Tolea, Krolik, & Tsvetanov 2002; Hewett & Foltz 2003). These analyses indicate that the true fraction of BALQSOs and BAL covering factors may be substantially larger ( $\gtrsim 20\%$ ) than the often quoted value of  $\sim 10\%$ .

The study of BALQSOs in the X-ray band may provide valuable information regarding the total column densities and the ionization equilibrium of the BAL absorber. X-

ray absorption in BALQSOs is expected to be largely due to photoelectric, bound-free absorption and is less sensitive to effects such as saturation and the degree of ionization, often encountered in optical and UV observations (e.g., Arav 1998). Because of the heavy X-ray absorption in BALQSOs, the X-ray spectra obtained to date have modest (e.g., PG 2112+059) to poor signal-to-noise (S/N) ratios and cannot accurately constrain the column densities, ionization state, geometry, or kinematic properties of BAL absorbers (e.g., Gallagher et al. 2001; Green et al. 2001; Gallagher et al. 2002). Furthermore, it is not clear whether the X-ray and UV absorbers are distinct.

Our recent *Chandra* observation of the BALQSO APM 08279+5255 indicated that quasars may contain winds with mass outflow rates considerably larger than previously thought (Chartas et al. 2002). This was suggested by the identification of two X-ray absorption features at rest-frame energies of 8.1 and 9.8 keV. By interpreting these features as resonant absorption lines of highly ionized Fe (e.g., Fe xxv  $K\alpha$ ), we inferred the presence of X-ray BAL material outflowing from the central source at velocities of  $\sim 0.2c$  and  $\sim 0.4c$ . Our analysis of APM 08279+5255 also suggested that the X-ray BAL material in this object is launched at radii of  $\lesssim 2 \times 10^{17}$  cm and therefore is likely not associated with the UV BAL material which is thought to be launched at larger radii. An observation of APM 08279+5255 performed with *XMM-Newton*  $\sim 1.8$  weeks (proper-time) after the *Chandra* ob-

<sup>1</sup> Department of Astronomy & Astrophysics, Pennsylvania State University, University Park, PA 16802. chartas@astro.psu.edu, niel@astro.psu.edu, scg@space.mit.edu

<sup>2</sup> MIT Center for Space Research, 77 Massachusetts Avenue, Cambridge, MA 02139.

servation showed an absorption feature near 7.4 keV (rest-frame) that was interpreted by Hasinger, Schartel, & Komossa (2002, hereafter H02) as a highly ionized iron edge (Fe xv–Fe xviii). If this interpretation is accepted an overabundance of Fe (factor  $\sim 2$ –5) is required to fit the *XMM-Newton* spectrum, assuming that the observed low and high-energy absorbers are the same. Recently, an ionized outflow with a velocity of 0.08–0.1c has also been detected in *XMM-Newton* observations of the narrow emission-line quasar PG 1211+143 (Pounds et al. 2003). Interestingly, there are no detected UV BALs from PG 1211+143. Additional insight into the association between the X-ray and UV BAL material was recently provided by contemporaneous *Chandra* and *HST* STIS observations of the BALQSO PG 2112+059 (Gallagher et al. 2003). Significant differences in the variability of the X-ray and UV absorbers in PG 2112+059 suggest the distinct nature of the X-ray and UV BAL material.

The confirmation of relativistic X-ray absorbing outflows in most quasars would imply higher mass-outflow rates than those based on outflow velocities derived from UV BALs. Such outflowing winds could provide a significant contribution to the enrichment of the vicinities of the quasars and their host galaxies with high-metallicity material. To address the question of whether relativistic X-ray absorbing outflows are a common phenomenon in quasars, we performed a deep observation of PG 1115+080 ( $z = 1.72$ ,  $B = 16.1$ ) with *XMM-Newton*. PG 1115+080 is a well-suited object for probing the kinematics of quasar winds. The relatively small velocity spread observed for the UV absorption in PG 1115+080, compared to the typical range of 5,000 – 25,000 km s<sup>-1</sup> observed in BAL quasars, suggests that PG 1115+080 be classified as a mini-BALQSO (Turnshek 1988; Barlow, Hamann, & Sargent 1997).

The large flux magnification, estimated to be a factor of  $\sim 20$ –40 (e.g., Impey et al. 1998), produced by gravitational lensing provided a bright background source that allowed the detection of absorption features from the outflowing wind. Here we present constraints on the kinematic and ionization properties of the outflowing wind of PG 1115+080 and provide results from our investigation of variability of the X-ray BALs of PG 1115+080 and APM 08279+5255. Throughout this paper we adopt a  $\Lambda$ -dominated Universe with  $H_0 = 70$  km s<sup>-1</sup> Mpc<sup>-1</sup>,  $\Omega_\Lambda = 0.7$ , and  $\Omega_M = 0.3$ .

## 2. OBSERVATIONS AND DATA ANALYSIS

PG 1115+080 was observed for 62.6 ks on 2001 Nov 25 with *XMM-Newton*. It was also observed with *Chandra* on 2000 June 2 and 2000 Nov 3 for 26.8 ks and 10.0 ks, respectively. The spectral analysis of the *Chandra* observations were presented in Gallagher et al. (2002). In §3.2, we provide a comparison between the *XMM-Newton* and *Chandra* spectral results and include an update on the *Chandra* analysis of PG 1115+080 that incorporates a recently developed contamination model for the ACIS instrument.

No significant background flares were present during the *XMM-Newton* observation, and the average background rates for the European Photon Imaging Camera (EPIC) PN and MOS detectors in the 0.2–10 keV

band were  $4.4 \times 10^{-6}$  events s<sup>-1</sup> arcsec<sup>-2</sup> and  $8.3 \times 10^{-7}$  events s<sup>-1</sup> arcsec<sup>-2</sup>, respectively. We analyzed the data with the standard analysis software SAS 5.3. PG 1115+080 was clearly detected with the PN, MOS1, and MOS2. The total number of source counts detected in the 0.2–10 keV band was  $\sim 12,200$  counts for the PN detector and  $\sim 8,185$  counts for the combined MOS1 and MOS2 detectors (henceforth referred to as MOS1+2). Flux variability was detected at the  $> 90\%$  confidence level based on a Kolmogorov-Smirnov (K-S) test. The timescale of the flux variations is of order 1000 s. A description of the timing analysis and inferred constraints on the Hubble constant based on the estimated time delay between the lensed images is presented in a separate paper (Chartas et al. 2003). We filtered the PN and MOS data by selecting events with PATTERNS in the 0–4 and 0–12 ranges, respectively. The MOS1 and MOS2 event lists were combined using the SAS task `merge` to increase the S/N ratio of the extracted spectrum.

The extracted spectra of PG 1115+080 from the PN and MOS were grouped to obtain a minimum of 100 counts in each energy bin, allowing use of  $\chi^2$  statistics. Background spectra for the PN and MOS1+2 detectors were extracted from source-free regions near PG 1115+080. The PN and MOS1+2 spectra were then fitted simultaneously with a variety of models employing XSPEC version 11.2 (Arnaud 1996). We tested the sensitivity of our results to the selected background and source extraction regions by varying the locations of the background regions and varying the sizes of the source extraction regions. We did not find any significant change in the background-subtracted spectra. For all models we included Galactic absorption due to neutral gas with a column density of  $N_H = 3.53 \times 10^{20}$  cm<sup>-2</sup> (Stark et al. 1992). All quoted errors are at the 90% confidence level unless mentioned otherwise with all parameters taken to be of interest except absolute normalization.

We first simultaneously fitted the PN and MOS1+2 spectra of PG 1115+080 with a model consisting of a power law with neutral intrinsic absorption at  $z = 1.72$  (fit 1 of Table 1). This fit supports the presence of an intrinsic absorber with a column density of  $N_H = 2.7_{-0.5}^{+0.5} \times 10^{21}$  cm<sup>-2</sup>. The fit is not acceptable in a statistical sense [reduced  $\chi^2 = 1.54$  for 209 degrees of freedom (dof)]. The fit residuals show significant absorption from 2–5 keV that contributes to the unacceptable fit. To illustrate the presence of these features and the absorption features below 0.6 keV, we fit the spectrum between 1–2.6 keV and 5.2–10 keV with a power-law model modified by Galactic absorption and extrapolated this model to the energy ranges not fit (see Figure 1a). For clarity we only show the higher S/N ratio PN data in Figure 1; however, all fits were performed simultaneously to the PN and MOS1+2 data. In Figures 2a and 2b we show the  $\Delta\chi$  residuals between the best-fit absorbed power-law model and the PN and MOS1+2 spectra. The complex absorption features from 2–5 keV are detected in both the PN and MOS1+2 spectra.

We proceeded to model the 2–5 keV features with a variety of models. We first considered an absorbed power-law model with two cosmologically redshifted Gaussian absorption lines near the absorption features appearing at

energies of 2.7 and 3.6 keV (observed-frame). This fit is a significant improvement compared to the previous one at the  $> 99.99\%$  confidence level and yields a reduced  $\chi^2 = 1.33$  for 201 dof (fit 2 of Table 1). The addition of the two Gaussian lines significantly reduced the residuals, and the remaining most significant contribution to the large value of  $\chi^2$  arises from the residuals below 0.6 keV. These low-energy residuals are commonly detected in moderate S/N ratio X-ray spectra of BALQSOs and are thought to arise from ionized or partially covering intrinsic absorption (e.g., Gallagher et al. 2002). To test this we replaced the neutral absorber in our spectral model with an ionized intrinsic absorber (see fit 5 of Table 1). In particular, we used the `absori` model contained in `XSPEC` (Done et al. 1992). In Figure 1b we show the PN spectrum fit with this model and the residuals of this fit. We found a significant improvement in fit quality at the  $> 99.99\%$  confidence level (according to the  $F$ -test) with reduced  $\chi^2 = 1.16$  for 200 dof (see fit 5 of Table 1). The best-fit rest-frame energies and widths of the absorption features are  $E_{abs1} = 7.38^{+0.17}_{-0.10}$  keV,  $\sigma_{abs1} < 0.44$  keV and  $E_{abs2} = 9.5^{+0.9}_{-1.4}$  keV (68% confidence),  $\sigma_{abs2} = 2.4^{+1.2}_{-0.9}$  keV (68% confidence).<sup>3</sup>

Both of the 2–5 keV features occur in a well-calibrated energy region where the effective area of the combined telescope and instrument responses varies smoothly. The best-fit value for the photon index is  $\Gamma = 1.90^{+0.04}_{-0.04}$ , consistent with those of typical radio-quiet quasars. The ionized absorber is characterized by an ionization parameter of  $\xi = L/nr^2 = 101.4^{+58}_{-48}$  erg cm s<sup>-1</sup> and a hydrogen column density of  $N_{\text{H}} = 1.1^{+0.5}_{-0.4} \times 10^{22}$  cm<sup>-2</sup>, where  $L$  is the integrated 5 eV–300 keV incident luminosity,  $n$  is the number density of the absorber, and  $r$  is the distance between the absorber and ionizing source.

We also modeled the absorption from 2–5 keV with one and two absorption edges. The fit with one edge is slightly worse (at the 90% confidence level) than the fit that included the two Gaussian lines and yields a reduced  $\chi^2 = 1.18$  for 206 dof (fit 3 of Table 1). The best-fit edge energy and optical depth are  $E_{edge} = 7.07^{+0.20}_{-0.23}$  keV and  $\tau_{edge} = 0.31 \pm 0.12$ . An inspection of this fit shows that significant residuals are present from 2–5 keV. The fit with two absorption edges is comparable in quality to the fit that included two Gaussian absorption lines and yields a reduced  $\chi^2 = 1.16$  for 204 dof. The best-fit energies and optical depths of the two absorption edges are  $E_{edge1} = 7.03^{+0.19}_{-0.32}$  keV,  $\tau_{edge1} = 0.31 \pm 0.11$  and  $E_{edge2} = 9.63^{+0.77}_{-0.43}$  keV,  $\tau_{edge2} = 0.22 \pm 0.14$ . The best-fit values for the edge energies would imply that the first edge arises from nearly neutral Fe with a  $2\sigma$  confidence range from Fe I to Fe VII, whereas the second edge energy lies  $1\sigma$  above the threshold energy of the highest ionization level of Fe XXVI (9.278 keV). While the fit that incorporates two absorption edges is acceptable in a statistical sense, the inferred energies and optical depths are difficult to explain with a physically acceptable model (see §3.1). The multiple-edge model would imply that the detected high-energy absorption is produced by two distinct absorbers, one nearly neutral and the other highly ionized.

The optical depths of the edges imply hydrogen column densities of  $\sim 2.7 \times 10^{23}$  cm<sup>-2</sup> for the edge at 7.03 keV and  $\sim 6.9 \times 10^{23}$  cm<sup>-2</sup> for the edge at 9.63 keV (for solar abundances and adopting the threshold cross sections of Verner & Yakovlev 1995). In §3.1 we investigate whether spectral models that incorporate direct and scattered radiation from the central source can provide acceptable fits to the low and high-energy absorption features in the *XMM-Newton* spectrum of PG 1115+080.

### 3. DISCUSSION

Our *XMM-Newton* observation of PG 1115+080 has revealed a BALQSO with two absorption features very similar in rest-frame energy to the ones recently identified in *Chandra* observations of the BALQSO APM 08279+5255. In §3.1 we investigate three spectral models to explain these high-energy absorption features, provide constraints on their kinematic and ionization properties, and examine a possible connection between the low and high-energy absorbers. In §3.2 we investigate possible variability of these absorption features by comparing the *Chandra* and *XMM-Newton* observations of PG 1115+080 separated by 19 weeks (proper-time). We also briefly discuss the variability of similar absorption features detected in *Chandra* and *XMM-Newton* observations of APM 08279+5255 separated by 1.8 weeks (proper-time) and place constraints on the size and location of these absorbers.

#### 3.1. Origin and Properties of the X-ray Absorbers in PG 1115+080

We attempted to determine the origin of the low and high-energy absorption features seen from PG 1115+080 by considering the three following models:

(a) Our first model consisted of neutral and ionized absorption with variable metal abundances. The neutral component consisted of a power law modified by the `XSPEC` model `zvpabs` which assumes photoelectric absorption with variable abundances. The ionized component consisted of a power law modified by the `XSPEC` model `absori`. The Fe abundances of both components were allowed to vary during the spectral fits. This multi-component model was an attempt to account for the results of the spectral fits that assumed a two-edge model (described in §2) to fit the high-energy absorption features. We assumed that our lines of sight through the neutral and ionized absorber are different. This can occur if the observed spectrum consists of (1) direct absorbed and (2) scattered, absorbed emission from the central source. The fit with this multiple-component model was acceptable in a statistical sense yielding a reduced  $\chi^2 = 1.13$  for 202 dof. However, there are problems with explaining the resulting values for several of the parameters. First, the best-fit value of the Fe abundance needed to model the neutral absorption feature near  $\sim 7.1$  keV is  $\sim 425^{+335}_{-330}$  times solar, and the Fe abundance needed to model the ionized low-energy absorption is  $\sim 15 \pm 10$  times solar (errors are at the 90% confidence level). These values are unphysically large. Second, the  $\Delta\chi$  residuals of this fit indicate that the double line of sight model can fit the low-energy absorption well, but, significant residuals remain near the absorption feature at

<sup>3</sup> The unusually large width of the absorption line at 9.5 keV may be due to multiple unresolved narrower components. Higher resolution spectra are needed to resolve this issue.

9.6 keV. We considered the case where the ionized and neutral absorbers were along the same line of sight. The fit with this model was not acceptable in a statistical sense with a reduced  $\chi^2 = 1.26$  for 205 dof. The best-fit value of the column density of the neutral absorber for this model is  $N_{\text{H}} = 0.0^{+0.1}_{-0.0} \times 10^{21} \text{ cm}^{-2}$ .

(b) We also investigated whether intervening absorbers in the lens galaxy at  $z = 0.31$  or in possible damped Lyman alpha systems along the line of sight could explain the high-energy absorption features. Spectroscopic observations of PG 1115+080 in the UV have not detected any Lyman-limit discontinuities (Green et al. 1980; Tripp et al. 1990) and place an upper limit on the lens galaxy's column density of neutral hydrogen of  $N_{\text{H}} \lesssim 3 \times 10^{16} \text{ cm}^{-2}$ . The most abundant elements with K-shell threshold energies near the energies of the observed high-energy absorption features are Si and S. For the purpose of this investigation we compared the K-shell threshold energies of Si and S (corrected for the redshift of any intervening absorber between us and PG 1115+080) to the best-fit energies of  $E_{\text{edge}1} = 2.59 \text{ keV}$  and  $E_{\text{edge}2} = 3.54 \text{ keV}$  (observed-frame) obtained from our fits that assumed two absorption edges (see §2 and fit 4 of Table 1). The energies of the Si I – XIV and S I – XVI K-shell threshold energies range between 1.846–2.673 keV and 2.477–3.494 keV, respectively. We expect most of the Si and S in intervening damped Lyman alpha systems or in the lens galaxy to be neutral or mildly ionized. We find that all the K-shell threshold energies of Si and S fall significantly below the energies of the observed high-energy absorption features for absorption produced in the lens galaxy with the exception of S XVI which falls between the two observed high-energy absorption features. All ionization levels of Si and S are also ruled out as producing the absorption edge at 3.54 keV for any intervening absorber. We conclude that the observed high-energy absorption features cannot be produced by absorption in intervening systems or in the lens galaxy, and the most likely origin is intrinsic absorption by highly ionized iron.

(c) Finally, we examined a model that assumes the high-energy absorption features arise from different zones of a highly ionized outflowing wind. A similar model was used to explain the high-energy absorption features in the *Chandra* spectrum of APM 08279+5255. In particular, for the case of APM 08279+5255 we interpreted these features as two distinct absorption systems in the quasar outflow with velocities of  $\sim 0.2c$  and  $\sim 0.4c$ , respectively; however, see H02 for a different interpretation of the *XMM-Newton* spectrum of APM 08279+5255. For the *XMM-Newton* observations of PG 1115+080 we found that the absorption features are located at rest-frame energies of  $7.38^{+0.17}_{-0.10} \text{ keV}$  (90% confidence) and  $9.50^{+0.90}_{-1.40} \text{ keV}$  (68% confidence); see fit 5 of Table 1. Applying similar arguments to infer the nature of the lines in PG 1115+080 as those presented in Chartas et al. (2002) for APM 08279+5255, we conclude that the absorption lines detected from PG 1115+080 are most likely due to highly ionized Fe ions in the quasar wind. We estimate that the 7.38 keV and 9.50 keV absorption features correspond to wind velocities (depending on the ionization state of Fe) of  $0.10c$  (Fe XXV K $\alpha$ ),  $0.04c$  (Fe XXVI K $\alpha$ ) and  $0.34c$  (Fe XXV K $\alpha$ ),  $0.30c$  (Fe XXVI K $\alpha$ ) respectively,

relative to the systemic redshift of  $z = 1.72$ . For these velocity calculations we included the special relativistic velocity correction.

At the  $1\sigma$  level, the ratio of the two absorption-line energies ( $E_{\text{abs}1}/E_{\text{abs}2}$ ) is inconsistent with the ratio of the energies of the iron K $\alpha$  to K $\beta$  transitions of Fe XXV and Fe XXVI. The predicted ratio of  $EW_{\text{abs}2}/EW_{\text{abs}1}$  of the two high-energy absorption lines is  $\sim 7.1$  (7.4) assuming that these lines are the iron K $\alpha$  and K $\beta$  transitions of Fe XXV (Fe XXVI) and the absorption is on the linear part of the curve of growth. The observed ratio of  $EW_{\text{abs}1}/EW_{\text{abs}2} = 0.1 \pm 0.06$  is much less than the predicted ratio, and thus does not obviously support the iron K $\alpha$  and K $\beta$  interpretation of the high-energy absorption lines. We note, however, that in the likely case where the absorption lines are saturated or are composed of multiple unresolved components the observed  $EW_{\text{abs}2}/EW_{\text{abs}1}$  ratio could deviate significantly from the predicted ratio assuming the iron K $\alpha$  and K $\beta$  interpretation. A second argument against the iron K $\alpha$  and K $\beta$  interpretation is the observed radical difference of the line profiles of the absorption lines at 7.38 keV and 9.50 keV (see fit 5 of Table 1) that is not expected if these absorption features are produced by iron K $\alpha$  to K $\beta$  transitions of Fe XXV or Fe XXVI.

UV spectra of PG 1115+080 acquired with the International Ultraviolet Explorer (*IUE*) reveal an O VI  $\lambda 1033$  resonant emission line accompanied by absorption in the line core and absorption features blueward of the line that extend over a velocity range of 0–6000  $\text{km s}^{-1}$  (Michalitsianos & Oliverson 1996). A possible explanation for the large differences between the UV and X-ray BAL wind velocities is that the two absorbers are launched at different distances from the central ionizing source and are therefore accelerated to different terminal velocities. To examine this hypothesis further we estimated the wind velocity as a function of radius following §5 of Chartas et al. (2002). We assumed a minimum launching radius for the UV BAL absorber of  $r_{\text{min}} \sim 1 \times 10^{16} (M_{\text{bh}}/M_8)^{1/2} \text{ cm}$ , based on hydrodynamical simulations performed by Proga et al. (2000), where  $M_{\text{bh}}$  is the mass of the black hole of PG 1115+080 and  $M_8 = 10^8 M_{\odot}$ . In Figure 3 we plot the velocity of the UV absorber versus radius from the central source for launching radii of  $r_{\text{min}}$ ,  $2.5r_{\text{min}}$  and  $5r_{\text{min}}$ . We have assumed a force multiplier of  $\Gamma_f = 100$  (e.g., Arav, Li, & Begelman 1994),  $L_{\text{UV}} = 5 \times 10^{44} \text{ erg s}^{-1}$ ,  $L_{\text{Bol}} = 2 \times 10^{45} \text{ erg s}^{-1}$ , and  $L_{\text{Bol}}/L_{\text{Edd}} = 0.1$ . The terminal velocity of UV material launched at the minimum launching radius is  $\sim 0.07c$ , significantly less than the velocities of the X-ray BAL absorbers. As we proposed in the case of APM 08279+5255, a possible explanation for the larger velocities of the X-ray BAL absorbers is that this material is initially accelerated at smaller launching radii than the UV BAL material. The short recombination timescales of Fe XXV and/or Fe XXVI compared to the estimated time for the X-ray BAL material to be accelerated close to its terminal velocity imply that the observed highly ionized Fe is located near the launching radius where it would still be exposed to intense ionizing radiation from the central X-ray source. One of the implications of small launching radii for the X-ray BAL material is possible variability over timescales of weeks to months of the energies and

widths of the X-ray BALs as the ionized X-ray absorbers are accelerated to their terminal velocities.

We investigated a possible connection between the low and high-energy X-ray absorbers by comparing their kinematic, ionization, and absorbing properties. We searched for a possible outflow velocity of the low-energy absorber by allowing the redshift parameter of the ionized-absorber model to be free. The best-fit redshift of the absorber of  $z = 1.53_{-0.7}^{+0.6}$  (90% confidence errors) was consistent with the systemic value of  $z = 1.72$  (and also with the blue-shifted values of  $z = 1.46$  and  $0.92$  expected from the velocities of the high-energy absorbers), and we found no significant improvement in the low-energy fit residuals and no improvement in the global fit. We note, however, that if the low-energy absorber has a large velocity dispersion it would be difficult to detect a blue-shift. The estimated hydrogen column density of the low-energy absorber ranges from  $N_{\text{H}}=1.8 \times 10^{21} \text{ cm}^{-2}$  assuming the neutral absorption model (fit 2 of Table 1) to  $N_{\text{H}}=1.1 \times 10^{22} \text{ cm}^{-2}$  assuming the ionized absorber model (fit 5 of Table 1); we note that these  $N_{\text{H}}$  values may have significant systematic errors due to the inadequacy of the absorption models. Specifically, these models do not include effects such as possible velocity dispersion of the absorber, BALs, and multiple ionization zones. To obtain an estimate of the hydrogen column densities of the high-energy absorbers we performed a simple curve-of-growth analysis (Spitzer 1978) on the detected absorption features. For no ionization correction (assuming all of the Fe is in the Fe XXV ionization state) and assuming solar abundances, the total hydrogen column densities corresponding to the absorption lines at  $7.38_{-0.10}^{+0.17} \text{ keV}$  and  $9.50_{-1.40}^{+0.90} \text{ keV}$  are  $N_{\text{H}} = 4 \times 10^{22} \text{ cm}^{-2}$  and  $N_{\text{H}} = 4 \times 10^{23} \text{ cm}^{-2}$ , respectively. We consider these estimates of the column densities also to have likely systematic errors since the absorption lines may contain multiple unresolved absorption components leading to an overestimate of the column densities of individual velocity components and the  $b$  parameters obtained from fits of Gaussian lines to observed absorption features are valid only in the optically thin limit. On the other hand, possible saturation of the absorption lines will lead to an underestimate of the column densities. Our preliminary comparison of the kinematic properties of the low-energy and high-energy absorbers cannot conclusively show whether they are outflowing at similar velocities, however, our spectral analysis indicates that these absorbers have different ionization parameters. In particular, the best-fit ionization parameter for the low-energy absorption is  $\xi = 101_{-48}^{+58} \text{ erg cm s}^{-1}$  (see fit 5 of Table 1), whereas, the presence of highly ionized Fe (high-energy absorption features) requires  $\xi \gtrsim 1000 \text{ erg cm s}^{-1}$ . We therefore conclude that the low and high-energy absorbers of PG 1115+080 are likely distinct; however, higher spectral resolution is needed to confirm this result.

### 3.2. Variability of X-ray BALs in PG 1115+080 and APM 08279+5255

We searched for variability of the X-ray BALs of PG 1115+080 and APM 08279+5255 by comparing their properties at different epochs. We first compared the X-

ray spectra of PG 1115+080 obtained in *Chandra* and *XMM-Newton* observations separated by  $\sim 19$  weeks. We fit the *Chandra* spectrum obtained on 2000 June 2 for 26.8 ks simultaneously with the *XMM-Newton* spectrum of PG 1115+080 using the spectral model of fit 5 of Table 1. To account for the recently observed quantum efficiency decay of ACIS, possibly caused by molecular contamination of the ACIS filters, we have applied a time-dependent correction to the ACIS quantum efficiency implemented in the XSPEC model ACISABS1.1.<sup>4</sup> We allowed the normalization of the power-law component to be a free parameter in the fit to account for any flux variability and/or systematic calibration uncertainties between the *Chandra* and *XMM-Newton* instrumental efficiencies. We found a degradation in fit quality at the 90% confidence level compared to the fit of the same model to the *XMM-Newton* spectrum of PG 1115+080 based on the  $F$ -test. This change in fit quality is suggestive of variability of the spectrum of PG 1115+080.

When we repeated the fit to the *Chandra* spectrum of PG 1115+080 allowing the model parameters of the low and high-energy absorbers to vary, we obtain best-fit rest-frame line energies, widths, equivalent widths, and 68% confidence levels of the absorption features of  $E_{\text{abs}1} = 7.37_{-0.30}^{+0.14} \text{ keV}$ ,  $\sigma_{\text{abs}1} < 0.35 \text{ keV}$ ,  $EW_{\text{abs}1} = 96_{-73}^{+48} \text{ eV}$  and  $E_{\text{abs}2} = 8.5_{-0.2}^{+0.2} \text{ keV}$ ,  $\sigma_{\text{abs}2} < 0.25 \text{ keV}$ ,  $EW_{\text{abs}2} = 178_{-92}^{+121} \text{ eV}$ . The best-fit values for the ionization parameter and hydrogen column density of the low-energy ionized absorber during the *Chandra* observation are  $\xi = 398_{-210}^{+260} \text{ erg cm s}^{-1}$  and  $N_{\text{H}} = 3.2_{-1.5}^{+2.1} \times 10^{22} \text{ cm}^{-2}$ . A comparison between the *Chandra* and *XMM-Newton* observations indicates that the line width of the second absorption feature varied to  $\sigma_{\text{abs}2} = 2.4_{-0.9}^{+1.2} \text{ keV}$  for the *XMM-Newton* observation. The properties of the absorption line at  $E_{\text{abs}1} = 7.4 \text{ keV}$  were consistent between both observations. In Figures 4a and 4b we show the  $\Delta\chi$  residuals between the best-fit simple absorbed power-law model and the *XMM-Newton* PN and the *Chandra* ACIS spectra of PG 1115+080, respectively. The ionization parameter and hydrogen column density of the low-energy ionized absorber also appeared to vary to  $\xi = 101_{-48}^{+58} \text{ erg cm s}^{-1}$  and  $N_{\text{H}} = 1.1_{-0.4}^{+0.5} \times 10^{22} \text{ cm}^{-2}$  for the *XMM-Newton* observations. In Figures 5a and 5b we show the 68% and 90% confidence contours of photon index versus intrinsic low energy absorption column density and ionization parameter versus intrinsic column density for the *XMM-Newton* and *Chandra* observations assuming fit 5 of Table 1. These contours indicate a possible change (at the 68% confidence level) of the intrinsic column density and the ionization parameter between observations. To illustrate the significance of variability in the high-energy absorption features detected in PG 1115+080 with *XMM-Newton* and *Chandra* we present in Figures 6a and 6b confidence contours of  $E_{\text{abs}2}$  vs.  $\sigma_{\text{abs}2}$  and  $E_{\text{abs}2}$  vs. line-flux, respectively. We note, however, that these confidence contours are only suggestive of variability in the width and line flux of the absorption line at  $E_{\text{abs}2}$  since this line is only detected at the 68% confidence level in the *Chandra* spectrum of PG 1115+080. Flux and possibly spectral variability in

<sup>4</sup> ACISABS is an XSPEC model contributed to the *Chandra* users software exchange world wide web-site <http://asc.harvard.edu/cgi-gen/contsoft/soft-list.cgi>

the 0.2 – 1.0 keV band have been detected in earlier observations of this object performed with the *Einstein* IPC and *ROSAT* PSPC on 1979 Dec 10 and 1991 Nov 21, respectively (see Figures 5 and 6 of Chartas 2000). Specifically, the 0.2–2 keV flux varied from  $6.5 \times 10^{-13} \text{ erg s}^{-1} \text{ cm}^{-2}$  to  $0.4 \times 10^{-13} \text{ erg s}^{-1} \text{ cm}^{-2}$  between the *Einstein* IPC and *ROSAT* PSPC observations. The 0.2–2 keV and 0.2–10 keV fluxes of PG 1115+080 observed with the PN are  $2.7 \times 10^{-13} \text{ erg s}^{-1} \text{ cm}^{-2}$  and  $6.1 \times 10^{-13} \text{ erg s}^{-1} \text{ cm}^{-2}$ , respectively.

We also searched for variability of the X-ray absorption lines recently detected in *Chandra* and *XMM-Newton* observations of the BALQSO APM 08279+5255. The *Chandra* and *XMM-Newton* spectra were fit with model 5 of Table 1. Both fits were acceptable with reduced  $\chi^2 = 1.04$  for 102 dof in the *Chandra* case and reduced  $\chi^2 = 1.04$  for 116 dof in the *XMM-Newton* case. A comparison between the two observations separated by  $\sim 1.8$  weeks (proper-time) indicates that the values (quoted with 68% confidence errors) of  $E_{abs1} = 8.05^{+0.05}_{-0.04} \text{ keV}$ ,  $\sigma_{abs1} < 0.1 \text{ keV}$ ,  $E_{abs2} = 9.8^{+0.1}_{-0.1} \text{ keV}$ , and  $\sigma_{abs2} = 0.44^{+0.1}_{-0.1} \text{ keV}$  observed during the *Chandra* observations of APM 08279+5255 varied to  $E_{abs1} = 8.15^{+0.18}_{-0.14} \text{ keV}$ ,  $\sigma_{abs1} = 0.6^{+0.2}_{-0.2} \text{ keV}$ ,  $E_{abs2} = 11.0^{+0.7}_{-0.7} \text{ keV}$ , and  $\sigma_{abs2} = 2.0^{+0.3}_{-0.4} \text{ keV}$  for the *XMM-Newton* observations. In Figures 7a and 7b we show the  $\Delta\chi$  residuals between the best-fit simple absorbed power-law model and the *XMM-Newton* PN and *Chandra* ACIS spectra, respectively. The detection of significant variability of the widths and energies of the high-energy absorption lines in APM 08279+5255 confirms the intrinsic origin of the high-energy absorption features in this BALQSO (e.g., Hamann et al. 1995). The fact that the two absorption lines were narrower during the *Chandra* observation than during the *XMM-Newton* observation of APM 08279+5255 may explain why these features were more easily detectable in the former case. We conclude that the observed variability of the energies and widths of the X-ray BALs in APM 08279+5255 over a timescale of 1.8 weeks (proper-time) supports our earlier conclusion that these absorbers are most likely launched at relatively small radii of less than  $10^{16} (M_{bh}/M_8)^{1/2} \text{ cm}$ .

To summarize, we have reported the detection of a relativistic outflow in the BALQSO PG 1115+080 imprinted as resonant X-ray absorption lines at rest-frame energies of  $7.38^{+0.17}_{-0.10} \text{ keV}$  (90% confidence) and  $9.50^{+0.90}_{-1.40} \text{ keV}$  (68% confidence). These energies suggest the presence of two distinct absorbers outflowing at velocities of  $\sim 0.10c$  and  $\sim 0.34c$ . We found significant variability of the properties of the X-ray BALs in APM 08279+5255 over a period of 1.8 weeks (proper-time) supporting our earlier conclusion that X-ray BALs are launched at relatively small radii compared to the expected UV BAL minimum launching radii.

Resolving the low and high-energy absorption features seen from PG 1115+080 and APM 08279+5255 is required to constrain better the kinematic, ionization, and absorbing properties of the observed outflows. The X-ray calorimeter onboard the ASTRO-E2 satellite (scheduled to launch in early 2005) has an effective area that is  $\approx 4$  times larger than that of the *Chandra* gratings in the energy range of the observed X-ray BALs and an energy resolution of about 12 eV. Future observations of PG 1115+080

and APM 08279+5255 with ASTRO-E2 may provide high-resolution spectra of X-ray BALs with exposure times of  $\approx 300 \text{ ks}$ . The current plan for the *Constellation – X* observatory calls for a combination of four satellites that will provide the higher energy resolution and larger effective area that is needed to resolve the complex structure of the X-ray BALs in PG 1115+080 and APM 08279+5255 with efficient exposure times of about 10 ks. In addition, monitoring of the X-ray BALs with *Constellation – X* on short timescales of the order of days may allow us to track the acceleration phase of the absorbers via the velocity shifts of the resonant absorption lines.

We thank those involved with the *XMM-Newton* Guest Observer Facility for assisting in the initial data reduction of PG 1115+080. We acknowledge financial support from NASA grant NAG5-9949. WNB acknowledges financial support from NASA LTSA grant NAG5-13035 and NASA grant NAG5-9932.

## REFERENCES

- Arav, N., Li, Z., & Begelman, M. C. 1994, *ApJ*, 432, 62
- Arav, N., Barlow, T. A., Laor, A., Sargent, W. L. W., & Blandford, R. D. 1998, *MNRAS*, 297, 990
- Arnaud, K. A. 1996, *ASP Conf. Ser. 101: Astronomical Data Analysis Software and Systems V*, 5, 17
- Barlow, T. A., Hamann, F., & Sargent, W. L. W. 1977, in *ASP Conf. Ser. 28, Mass Ejection from AGN*, ed. N. Arav, I. Shlosman, & R. J. Weymann, (San Francisco:ASP), 13
- Chartas, G. 2000, *ApJ*, 531, 81
- Chartas, G., Brandt, W. N., Gallagher, S. C., & Garmire, G. P. 2002, *ApJ*, 579, 169
- Chartas, G., Dai, X., & Garmire, G. P. 2003, *Carnegie Observatories Astrophysics Series, Vol. 2: Measuring and Modeling the Universe*, ed. W. L. Freedman (Pasadena: Carnegie Observatories, <http://www.ociw.edu/ociw/symposia/series/symposium2/proceedings.html>)
- Done, C., Mulchaey, J. S., Mushotzky, R. F., & Arnaud, K. A. 1992, *ApJ*, 395, 275
- Gallagher, S. C., Brandt, W. N., Laor, A., Elvis, M., Mathur, S., Wills, B. J., & Iyomoto, N. 2001, *ApJ*, 546, 795
- Gallagher, S. C., Brandt, W. N., Chartas, G., & Garmire, G. P. 2002, *ApJ*, 567, 37
- Gallagher, S. C., Brandt, W. N., Chartas, G., Garmire, G. P., & Sambruna, R. M., 2003, *Adv. Space Res.*, in press, astro-ph/0212304
- Goodrich, R. W. 1997, *ApJ*, 474, 606
- Green, P. J., Aldcroft, T. L., Mathur, S., Wilkes, B. J., & Elvis, M. 2001, *ApJ*, 558, 109
- Green, R. F., Pier, J. R., Schmidt, M., Estabrook, F. B., Lane, A. L., & Wahlquist, H. D. 1980, *ApJ*, 239, 483
- Hamann, F., Barlow, T. A., Beaver, E. A., Burbidge, E. M., Cohen, R. D., Junkkarinen, V., & Lyons, R. 1995, *ApJ*, 443, 606
- Hasinger, G., Schartel, N., & Komossa, S. 2002, *ApJ*, 573, L77 (H02)
- Hewett, P. C. & Foltz, C. B. 2003, in press *AJ*, astro-ph/0301191
- Impey, C. D., Falco, E. E., Kochanek, C. S., Lehár, J., McLeod, B. A., Rix, H.-W., Peng, C. Y., & Keeton, C. R. 1998, *ApJ*, 509, 551
- Krolik, J. H. & Voit, G. M. 1998, *ApJ*, 497, L5
- Michalitsianos, A. G., Oliverson, R. J., & Nichols, J. 1996, *ApJ*, 461, 593
- Proga, D., Stone, J. M., & Kallman, T. R. 2000, *ApJ*, 543, 686
- Spitzer, L. 1978, *Physical Processes in the Interstellar Medium* (New York: Wiley)
- Stark, A. A., Gammie, C. F., Wilson, R. W., Bally, J., Linke, R. A., Heiles, C., & Hurwitz, M. 1992, *ApJS*, 79, 77
- Tolea, A., Krolik, J. H., & Tsvetanov, Z. 2002, *ApJ*, 578, L31
- Tripp, T. M., Green, R. F., & Bechtold, J. 1990, *ApJ*, 364, L29
- Turnshek, D. A., Foltz, C. B., Grillmair, C. J., & Weymann, R. J., 1988, *ApJ*, 325, 651
- Verner, D. A. & Yakovlev, D. G. 1995, *A&AS*, 109, 125
- Weymann, R. J., Morris, S. L., Foltz, C. B., & Hewett, P. C. 1991, *ApJ*, 373, 23

TABLE 1  
RESULTS FROM FITS TO THE *XMM-Newton* SPECTRUM OF PG 1115+080

Fit <sup>a</sup>	Model	Parameter <sup>b</sup>	Value <sup>c</sup>
1	PL, neutral absorption at source.	$\Gamma$	$1.91^{+0.03}_{-0.03}$
		$N_{\text{H}}$	$(0.27^{+0.05}_{-0.05}) \times 10^{22} \text{ cm}^{-2}$
		$\chi^2/\nu$	322.7/209
		$P(\chi^2/\nu)^d$	$7.1 \times 10^{-7}$
2	PL, neutral absorption at source, and two Gaussian absorption lines at source.	$\Gamma$	$1.76^{+0.04}_{-0.04}$
		$N_{\text{H}}$	$(0.18^{+0.05}_{-0.05}) \times 10^{22} \text{ cm}^{-2}$
		$E_{\text{abs1}}$	$7.42^{+0.5}_{-0.2} \text{ keV}$
		$\sigma_{\text{abs1}}$	$< 0.55 \text{ keV}$ (68% errors)
		$EW_{\text{abs1}}$	$0.15^{+0.33}_{-0.11} \text{ keV}$
		$E_{\text{abs2}}$	$9.9^{+0.7}_{-0.9} \text{ keV}$
		$\sigma_{\text{abs2}}$	$3.0^{+0.6}_{-0.5} \text{ keV}$ (68% errors)
		$EW_{\text{abs2}}$	$2.2^{+1.0}_{-0.8} \text{ keV}$
		$\chi^2/\nu$	267.4/201
		$P(\chi^2/\nu)^d$	$1.2 \times 10^{-3}$
3	PL, ionized absorption at source and absorption edge.	$\Gamma$	$1.94^{+0.05}_{-0.03}$
		$N_{\text{H}}$	$(1.2^{+0.5}_{-0.4}) \times 10^{22} \text{ cm}^{-2}$
		$\xi$	$103^{+58}_{-45} \text{ erg cm s}^{-1}$
		$E_{\text{edge}}$	$7.07^{+0.20}_{-0.23} \text{ keV}$
		$\tau_{\text{edge}}$	$0.31^{+0.12}_{-0.11}$
		$\chi^2/\nu$	243.2/206
		$P(\chi^2/\nu)^d$	0.04
4	PL, ionized absorption at source and two absorption edges.	$\Gamma$	$1.88^{+0.05}_{-0.02}$
		$N_{\text{H}}$	$(1.0^{+0.5}_{-0.4}) \times 10^{22} \text{ cm}^{-2}$
		$\xi$	$91^{+60}_{-46} \text{ erg cm s}^{-1}$
		$E_{\text{edge1}}$	$7.03^{+0.19}_{-0.32} \text{ keV}$
		$\tau_{\text{edge1}}$	$0.31^{+0.11}_{-0.11}$
		$E_{\text{edge2}}$	$9.63^{+0.77}_{-0.43} \text{ keV}$
		$\tau_{\text{edge2}}$	$0.22^{+0.14}_{-0.14}$
		$\chi^2/\nu$	236.1/204
		$P(\chi^2/\nu)^d$	0.06
		5	PL, ionized absorption at source, and two Gaussian absorption lines at source.
$N_{\text{H}}$	$(1.1^{+0.5}_{-0.4}) \times 10^{22} \text{ cm}^{-2}$		
$\xi$	$101^{+58}_{-48} \text{ erg cm s}^{-1}$		
$E_{\text{abs1}}$	$7.38^{+0.17}_{-0.10} \text{ keV}$		
$\sigma_{\text{abs1}}$	$< 0.44 \text{ keV}$		
$EW_{\text{abs1}}$	$0.14^{+0.06}_{-0.06} \text{ keV}$		
$E_{\text{abs2}}$	$9.50^{+0.9}_{-1.4} \text{ keV}$ (68% errors)		
$\sigma_{\text{abs2}}$	$2.4^{+1.2}_{-0.9} \text{ keV}$ (68% errors)		
$EW_{\text{abs2}}$	$1.4^{+0.6}_{-0.4} \text{ keV}$		
$\chi^2/\nu$	230.9/200		
$P(\chi^2/\nu)^d$	0.07		

<sup>a</sup>All model fits include Galactic absorption toward the source (Stark et al. 1992). All fits are performed on the combined spectrum of images A1, A2, B and C of PG 1115+080.

<sup>b</sup>All absorption-line parameters are calculated for the rest frame.

<sup>c</sup>All errors are for 90% confidence unless mentioned otherwise with all parameters taken to be of interest except absolute normalization.

<sup>d</sup> $P(\chi^2/\nu)$  is the probability of exceeding  $\chi^2$  for  $\nu$  degrees of freedom if the model is correct.

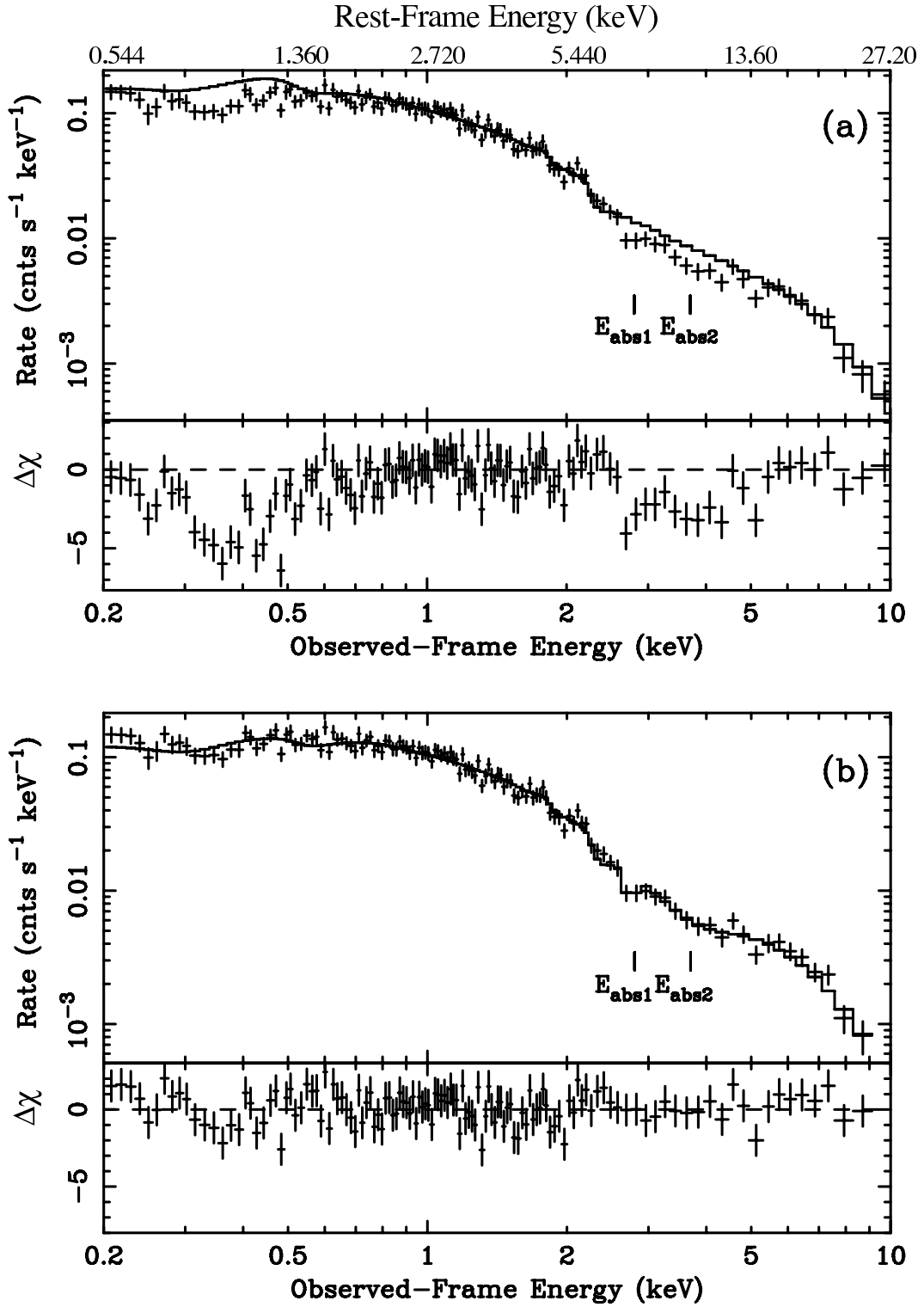


FIG. 1.— (a) The top panel shows the *XMM-Newton* PN spectrum of the combined images of PG 1115+080 fit with Galactic absorption and a power-law model to events with energies lying within the ranges of 1–2.6 keV and 5.2–10 keV. The lower panel shows the residuals of the fit in units of  $1\sigma$  deviations. Two absorption features from 2.6–5.2 keV are noticeable in the residuals plot. (b) The top panel shows the PN spectrum fit with Galactic absorption, ionized absorption at the source, a power-law model, and two Gaussian absorption lines. In the lower panel the residuals indicate that this model can account for most of the spectral features of PG 1115+080.

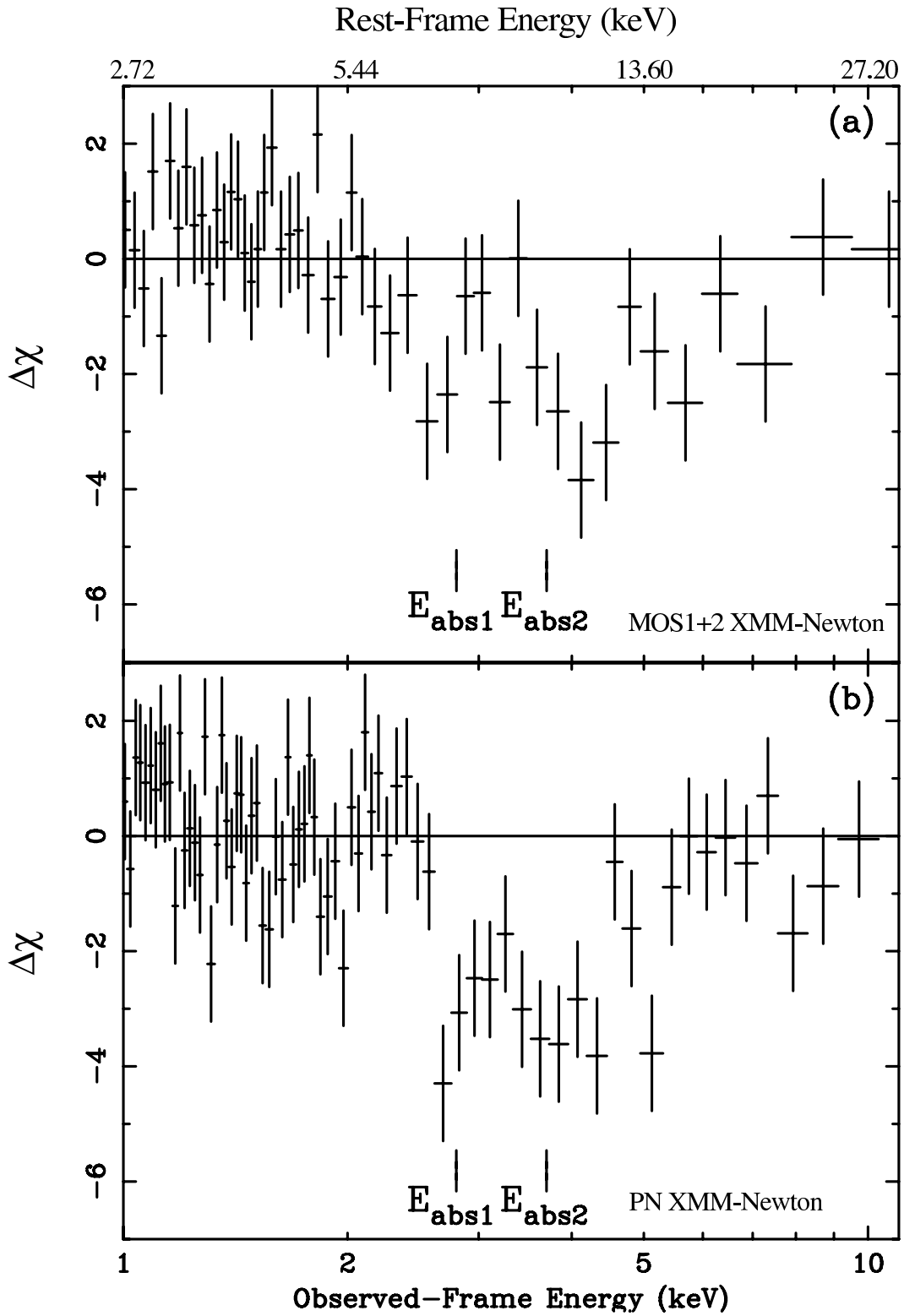


FIG. 2.—  $\Delta\chi$  residuals between the best-fit Galactic absorption and power-law model and (a) the MOS1+2 spectrum of PG 1115+080 and (b) the PN spectrum PG 1115+080. This model is fit to events with energies lying within the ranges 1–2.6 keV and 5.2–10 keV.  $E_{abs1}$  and  $E_{abs2}$  indicate the best-fit energies of the Gaussian absorption lines obtained in fit 5 of Table 1.

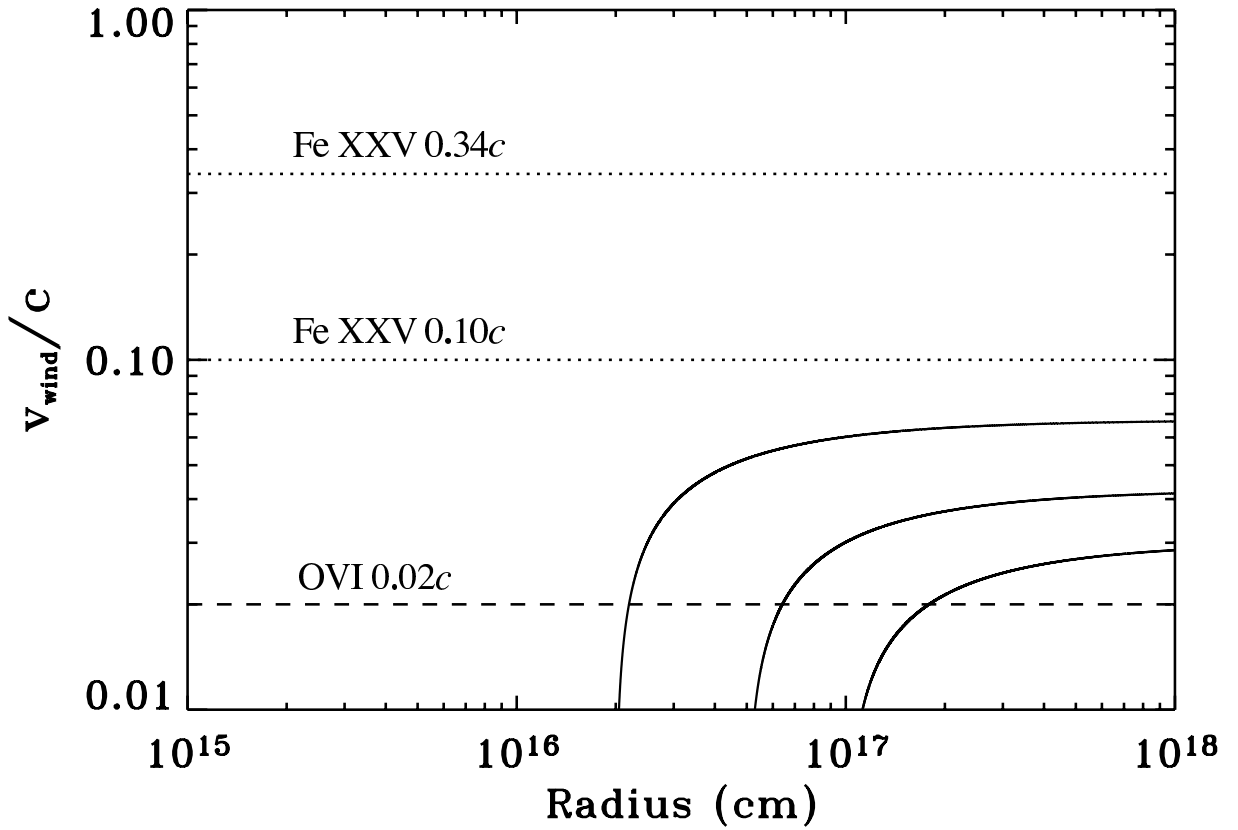


FIG. 3.— Wind velocity as a function of radius from the central source of PG 1115+080 for a radiation-pressure driven wind. For a qualitative comparison we have estimated the wind velocities for launching radii of  $2 \times 10^{16}$  cm,  $5 \times 10^{16}$  cm, and  $1 \times 10^{17}$  cm. We have over-plotted the observed O VI BAL (dashed line) and possible Fe XXV BAL (dotted lines) velocities.

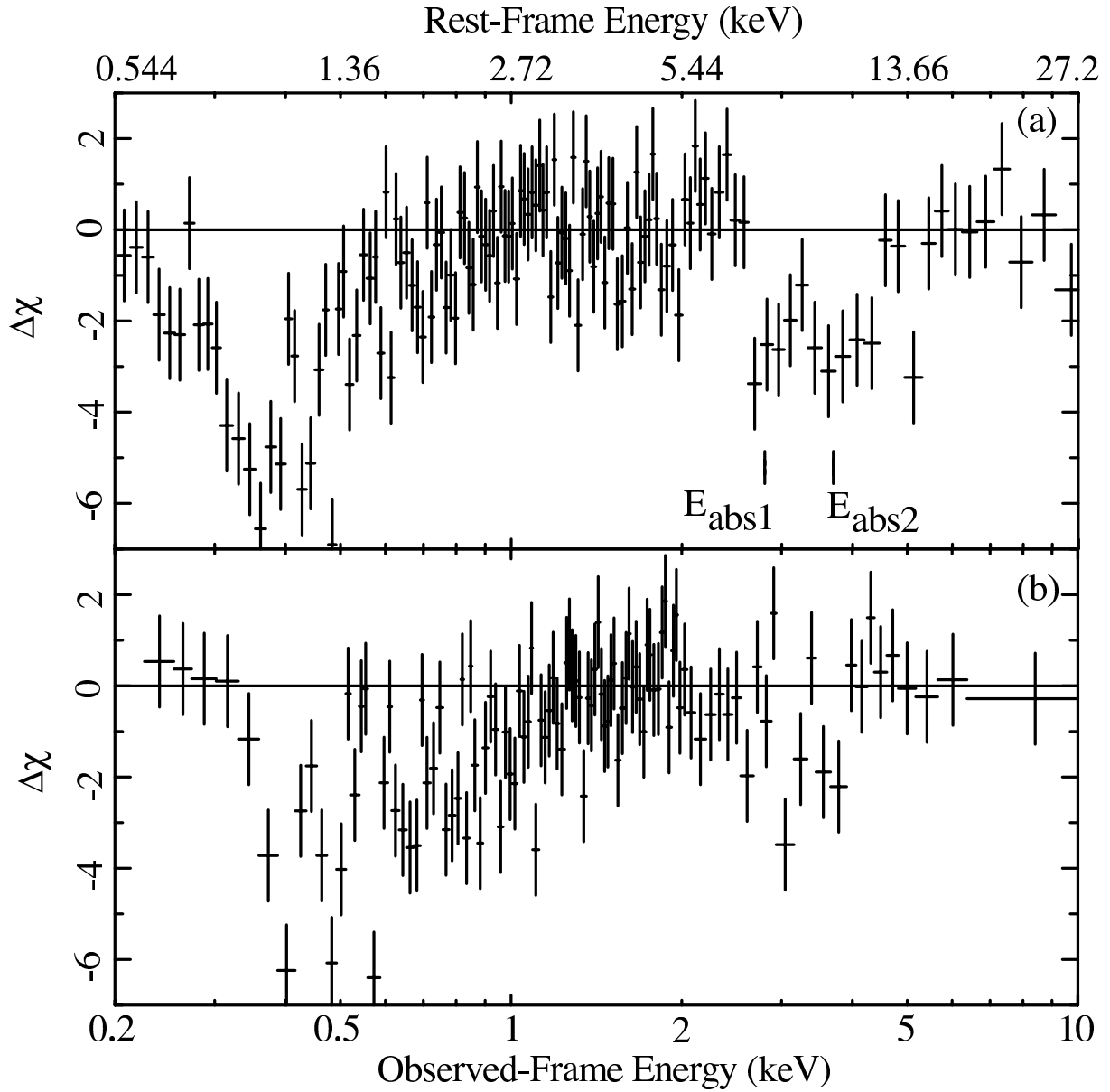


FIG. 4.—  $\Delta\chi$  residuals between the best-fit Galactic absorption and power-law model and (a) the *XMM-Newton* PN spectrum of PG 1115+080 and (b) the *Chandra* ACIS spectrum of PG 1115+080. The model has been fit to events with energies lying within the ranges of 1–2.6 keV and 5.2–10 keV.  $E_{abs1}$  and  $E_{abs2}$  indicate the best-fit energies of the Gaussian absorption lines obtained using the spectral model described in fit 5 of Table 1.

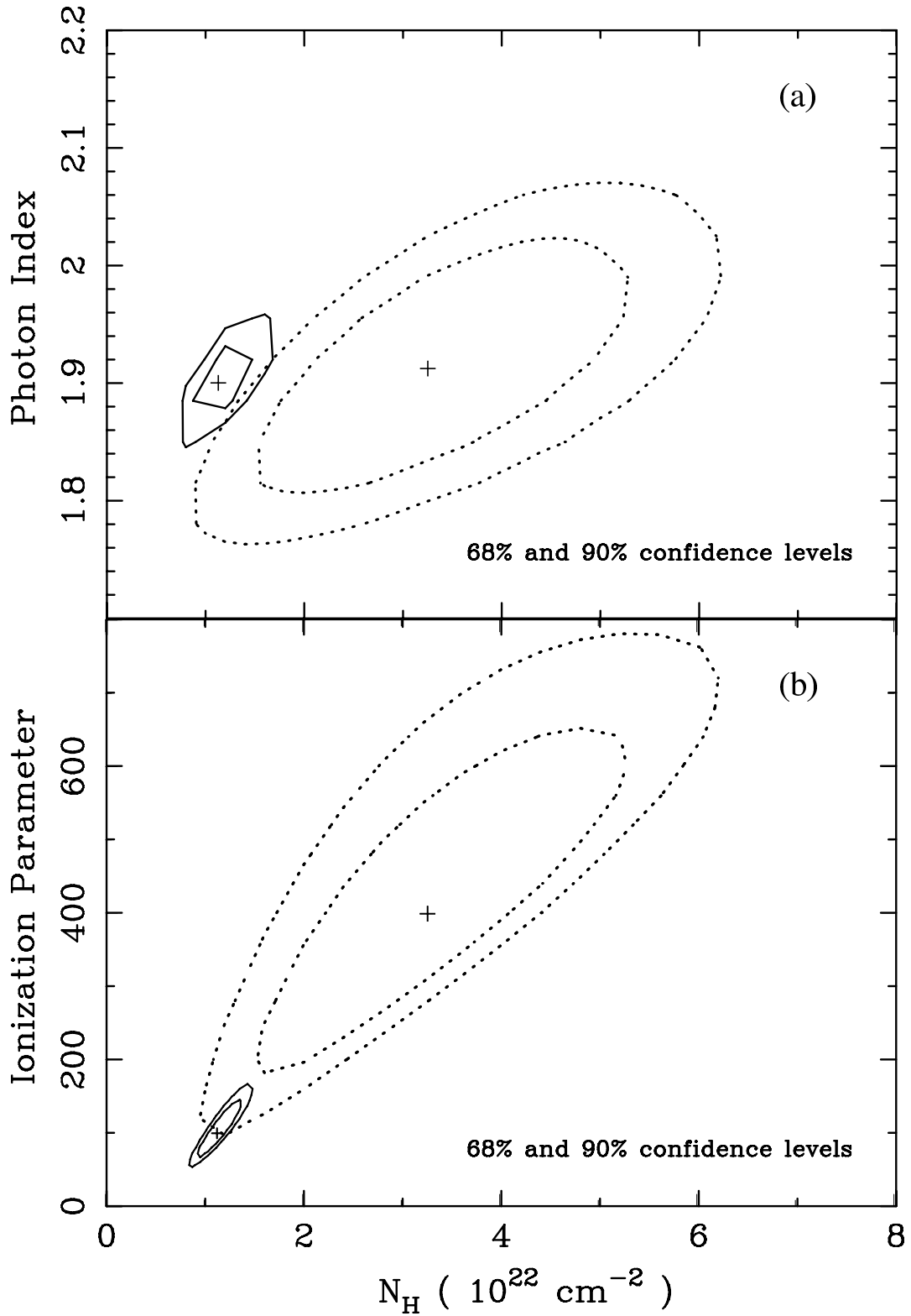


FIG. 5.— 68% and 90% confidence contours between (a) the spectral slope and the intrinsic absorption column density, and (b) the ionization parameter and the intrinsic absorption column density for the *XMM-Newton* (solid contours) and *Chandra* (dotted contours) observations of PG 1115+080 assuming fit 5 of Table 1.

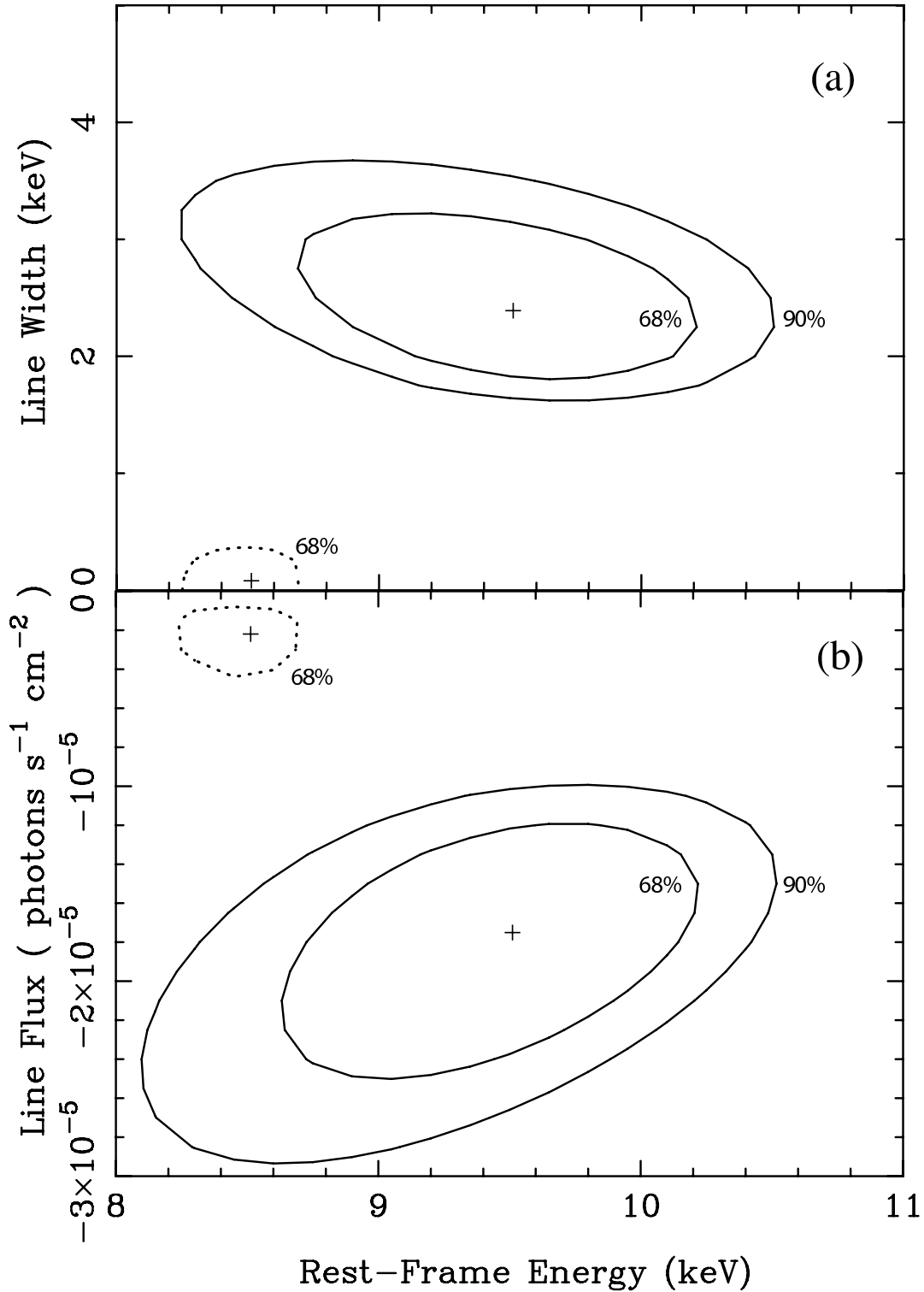


FIG. 6.— (a) 68% and 90% confidence contours between the width of the absorption feature at  $E_{abs2}$  and the energy  $E_{abs2}$  for the *XMM-Newton* (solid contours) and *Chandra* (dotted contours) observations of PG 1115+080 assuming fit 5 of Table 1. (b) 68% and 90% confidence contours between the flux of the absorption feature at  $E_{abs2}$  and the energy  $E_{abs2}$  for the *XMM-Newton* (solid contours) and *Chandra* (dotted contours) observations of PG 1115+080 assuming fit 5 of Table 1. These confidence contours are only suggestive of variability of the absorption line  $E_{abs2}$  between the *XMM-Newton* and *Chandra* observations since this absorption line is only detected at the 68% confidence level in the *Chandra* spectrum.

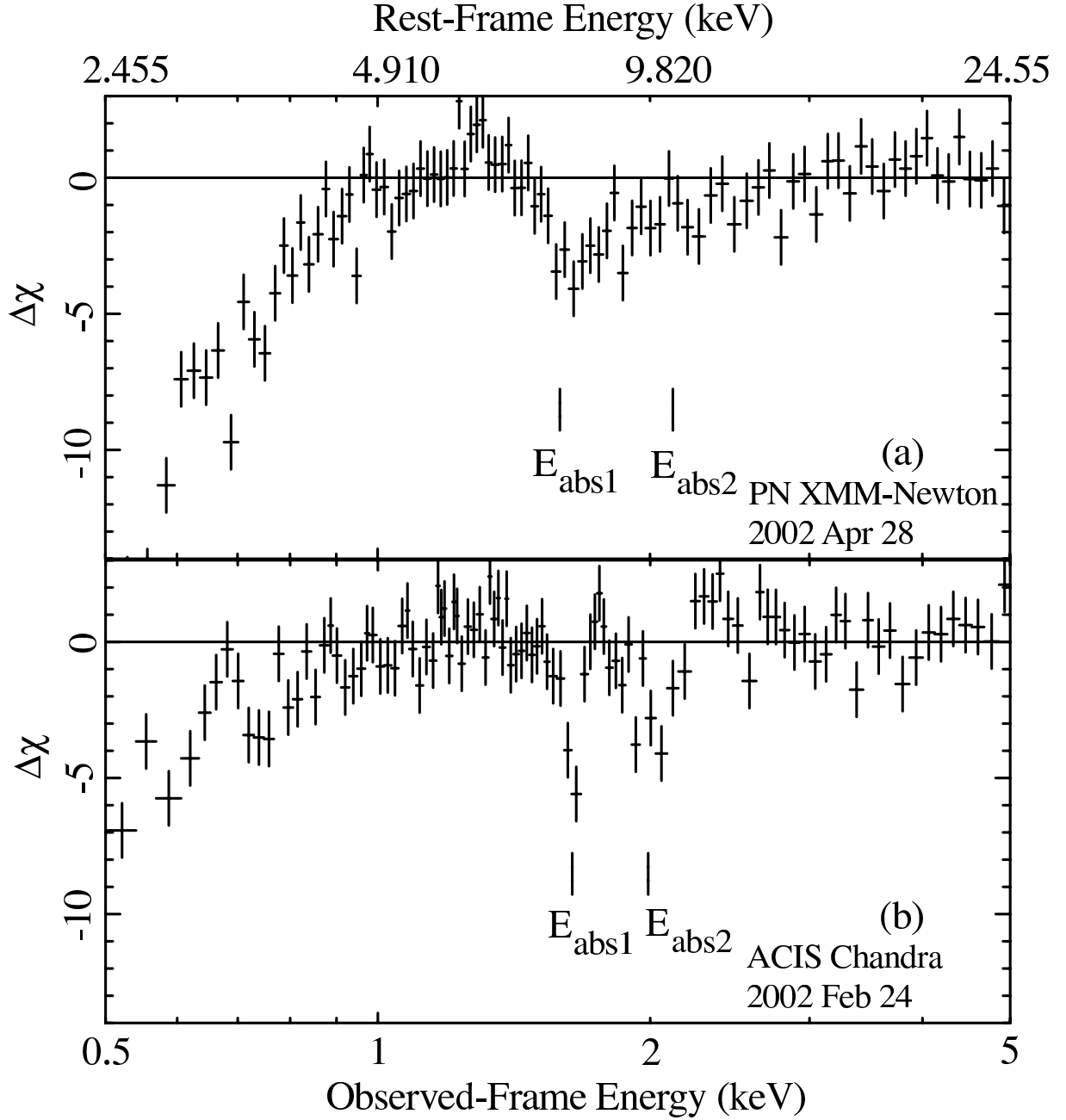


FIG. 7.—  $\Delta\chi$  residuals between the best-fit Galactic absorption and power-law model and (a) the *XMM-Newton* PN spectrum and (b) the *Chandra* ACIS spectrum of APM 08279+5255. This model is fit to events with energies lying within the range 2.2–10 keV.  $E_{\text{abs1}}$  and  $E_{\text{abs2}}$  indicate the best-fit energies of the Gaussian absorption lines obtained using the spectral model described in fit 5 of Table 1.